SCIENCE CHINA
Chemistry

•ARTICLES•

March 2020 Vol.63 No.3: 361–369
https://doi.org/10.1007/s11426-019-9670-2

Altering alkyl-chains branching positions for boosting the performance of small-molecule acceptors for highly efficient nonfullerene organic solar cells

Zhenghui Luo[1,2†], Rui Sun[3†], Cheng Zhong[2†], Tao Liu[1], Guangye Zhang[4], Yang Zou[1], Xuechen Jiao[5*], Jie Min[3*] & Chuluo Yang[1,2*]

[1]*Shenzhen Key Laboratory of Polymer Science and Technology, College of Materials Science and Engineering, Shenzhen University, Shenzhen 518060, China;*
[2]*Hubei Key Lab on Organic and Polymeric Optoelectronic Materials, Department of Chemistry, Wuhan University, Wuhan 430072, China;*
[3]*The Institute for Advanced Studies, Wuhan University, Wuhan 430072, China;*
[4]*eFlexPV Limited (China), Shenzhen, China;*
[5]*Department of Materials Science and Engineering, Monash University, Victoria, Australia*

Received November 04, 2019; accepted December 24, 2019; published online February 18, 2020

The emergence of the latest generation of small-molecule acceptor (SMA) materials, with Y6 as a typical example, accounts for the surge in device performance for organic solar cells (OSCs). This study proposes two new acceptors named Y6-C2 and Y6-C3, from judicious alteration of alkyl-chains branching positions away from the Y6 backbone. Compared to the Y6, the Y6-C2 exhibits similar optical and electrochemical properties, but better molecular packing and enhanced crystallinity. In contrast, the Y6-C3 shows a significant blue-shift absorption in the solid state relative to the Y6 and Y6-C2. The as-cast PM6:Y6-C2-based OSC yields a higher power conversion efficiency (PCE) of 15.89% than those based on the Y6 (15.24%) and Y6-C3 (13.76%), representing the highest known value for as-cast nonfullerene OSCs. Prominently, the Y6-C2 displays a good compatibility with the $PC_{71}BM$. Therefore, a ternary OSC device based on PM6:Y6-C2:$PC_{71}BM$ (1.0:1.0:0.2) was produced, and it exhibits an outstanding PCE of 17.06% and an impressive fill factor (FF) of 0.772. Our results improve understanding of the structure-property relationship for state-of-the-art SMAs and demonstrate that modulating the structure of SMAs via fine-tuning of alkyl-chains branching positions is an effective method to enhance their performance.

alkyl-chain branching position, small molecular acceptor, organic solar cell, power conversion efficiency, fill factor

Citation: Luo Z, Sun R, Zhong C, Liu T, Zhang G, Zou Y, Jiao X, Min J, Yang C. Altering alkyl-chains branching positions for boosting the performance of small-molecule acceptors for highly efficient nonfullerene organic solar cells. *Sci China Chem*, 2020, 63: 361–369, https://doi.org/10.1007/s11426-019-9670-2

1 Introduction

Non-fullerene small-molecule acceptors (SMAs) are gradually replacing fullerene derivatives in organic solar cells (OSC) due to their easily tunable optical and electronic properties [1–8]. In recent years, considerable efforts in molecular design and device engineering produced significant advances in the performance of SMA-based OSCs [9–26], with power conversion efficiencies (PCEs) above 16% [27–37] demonstrated in such nonfullerene devices. Generally, the rational design of nonfullerene SMAs focuses on the energetics and molecular interaction properties, aim-

†These authors contributed equally to this work.
*Corresponding authors (email: xuechen.jiao@monash.edu; min.jie@whu.edu.cn; clyang@whu.edu.cn)

© Science China Press and Springer-Verlag GmbH Germany, part of Springer Nature 2020

ing to optimize/balance the energy levels, the absorption spectra, and the crystallization/aggregation tendency [38–44]. Mainstream molecular design strategies include backbone modification, terminal unit, alteration, and side-chain engineering. Compared to backbone modification and terminal unit alteration, the "side-chain engineering" method fine-tunes the molecular properties and thus device performance and eliminates time-consuming synthesis [45–47]. Notably, subtle changes in side-chain structures facilitate understanding of the structure-property-performance relationships. The alteration of side chains including changes in symmetry [48], dimension [49], and length [33] can substantially influence the intermolecular interaction and crystalline behaviors of SMAs. For example, the SMA named IDT-OB, possessing asymmetric side chains, exhibits a higher device performance relative to that without symmetric side chains [48]. The side-chain conjugation strategy is employed to suppress excessive aggregation of molecules named ITIC1, thereby allowing the ITIC2 molecule to achieve a PCE above 11% [49]. In addition, by extending the side chains of the Y6, an SMA named BTP-4F-12 was developed, with good potential for large-scale industrial production using eco-compatible solvents [33].

Although the side-chain engineering strategy has been extensively employed, studies on the effect of the alkyl-chains branching positions on the property and performance of SMAs in OSCs remain scant [22]. Tuning alkyl-chains branching positions is an effective method for enhancing molecular packing and charge carrier mobility in organic field effect transistors (OFETs) [50–53]. For instance, McCulloch *et al.* [52] reported two new DPPTT-T-based copolymers by modifying the alkyl-chain branching point to improve molecular crystallinity and packing, thus achieving a better OFET performance. Regarding design, changing the alkyl-chains branching positions in SMAs is a potentially useful approach for improving the performance of OSCs, with the current surge of high-performance SMAs providing an ideal platform.

Herein, we choose the state-of-the-art SMA named Y6 [23] (or Y6-C1) as the control molecule, moving the branching points of the alkyl chains on the nitrogen atom to produce two novel acceptors named Y6-C2 and Y6-C3 (Scheme 1). In the scheme, C*n* represents the number of linear carbon atoms between alkyl-chain branching points and the alkylated nitrogen atom. Through systematic characterization, we demonstrate similar optical and electrochemical properties between the Y6-C2 and the Y6, with better molecular packing and enhanced crystallinity than Y6 from grazing incidence wide angle X-ray scattering (GIWAXS) results. In contrast, the Y6-C3 shows significantly blue-shifted absorption spectra in the solid state relative to the Y6 and Y6-C2. In addition, unlike the Y6 and Y6-C2, it adopts an edge-on orientation that is unfavorable for vertical charge transport and charge collection. When the two new molecules are introduced into devices, the as-cast OSCs based on the Y6-C2 and PM6 (Figure 1(a)) (donor polymer) yields a higher PCE (15.89%) than those based on the Y6 (15.24%) and Y6-C3 (13.76%). The PCE of 15.89% is the

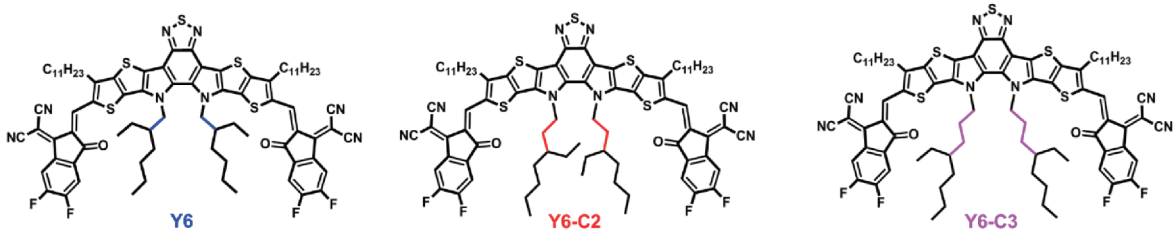

Scheme 1 Chemical structures of the acceptors of Y6, Y6-C2, and Y6-C3 (color online).

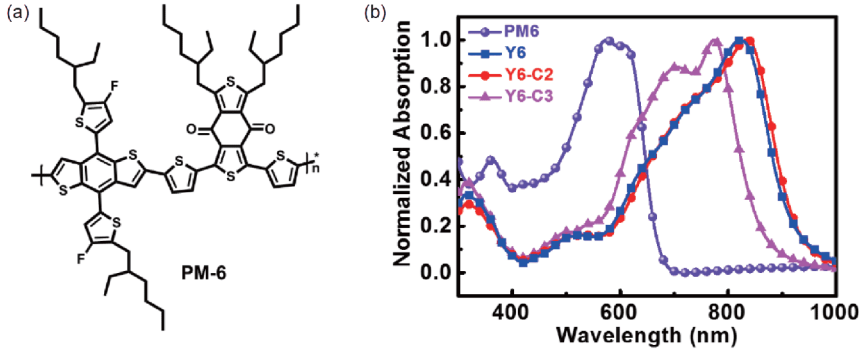

Figure 1 (a) Chemical structure of PM6, the donor polymer used in this study; (b) normalized UV-Vis absorption spectra of the PM6, Y6, Y6-C2, and Y6-C3 in neat film (color online).

highest known value for as-cast nonfullerene OSCs. Importantly, since the Y6-C2 shows good compatibility with the $PC_{71}BM$, a ternary device based on PM6:Y6-C2:$PC_{71}BM$ (1.0:1.0:0.2, weight ratio) is produced, and it yields a PCE reaching 17.06% and fill factor (FF) of 0.772. These results indicate that fine-tuning of alkyl-chains branching points is a suitable approach for producing highly efficient SMAs.

2 Results and discussion

The Supporting Information online (SI) contains descriptions showing that the Y6-C2 and Y6-C3 are efficiently synthesized according to Scheme S1. Compound 1 was involved in the classical double intramolecular Cadogan reductive cyclization reaction, while the intermediate passed through the nucleophilic substitution reaction in alkaline conditions to yield compound 2 (or compound 4). The Vilsmeier-Haack reaction was employed to form the double formyl groups of compound 3 (or compound 5). Finally, the Y6-C2 (or Y6-C3) was synthesized through the Knoevenagel condensation reaction between compound 3 (or compound 5) and 2-(5,6-difluoro-3-*oxo*-2,3-dihydro-1*H*-inden-1-ylidene) malononitrile (2FIC). The chemical structures of the intermediates and the target products were fully characterized by ^{1}H NMR, ^{13}C NMR, and matrix-assisted laser desorption/ionization time of flight mass spectrometry (MALDI-TOF). The two acceptors exhibit good solubility in commonly used organic solvents including dichloromethane (DCM), chloroform (CF), and chlorobenzene (CB).

The ultraviolet visible (UV-Vis) absorption spectra were measured for Y6, Y6-C2, and Y6-C3 in a dilute CF solution (Figure S1, Supporting Information online) and in a thin-film state (Figure 1(b)). The three acceptors display similar absorption spectra but different relative intensities of the 0-0 vibrational peaks in the dilute CF solution, suggesting different aggregation properties. Interestingly, the absorptions of both molecules containing short alkyl-chains (Y6 and Y6-C2) display obvious red shifts by ~95 nm from the solution to film. In contrast, the Y6-C3 shows a redshift of only ~45 nm. Compared with the Y6-C3, the alkyl-chains branching points of the Y6 and Y6-C2 are near the core, risking the suppression of core-to-core interaction, and benefiting the formation of J-aggregates (end-to-end arrangement of molecules) [54,55]. Conversely, for Y6-C3, the alkyl-chains branching points are far from the core, which is conducive for the formation of H aggregations (core-to-core arrangement). Therefore, the Y6 and Y6-C2 show distinct redshifted absorption in the solid state relative to Y6-C3. Consequently, the absorption edges of Y6, Y6-C2, and Y6-C3 in the solid state are 930, 932, and 880 nm, respectively, with corresponding optical bandgaps of 1.33, 1.33, and 1.41 eV. The narrower bandgap of the Y6 and Y6-C2 is beneficial for obtaining a higher short-circuit current density (J_{SC}) due to better complementary absorption with the polymer.

The energy levels of the Y6, Y6-C2, and Y6-C3 were determined by cyclic voltammetry (Figure 1(b) and Table 1). All acceptors exhibit similar lowest unoccupied molecular orbital (LUMO) ranging from −4.09 to −4.07 eV and highest occupied molecular orbital (HOMO) levels varying from −5.68 to −5.65 eV, demonstrating that tuning of the alkyl-chains branching points minimally influences electrochemical properties of the acceptors.

To explore the positions of the alkyl-chains relative to the π-conjugated backbone, a conformation search was performed using the following protocol: the initial conformers were obtained by systematic scanning of all rotatable bonds between the nitrogen atom and the tertiary carbon on the alkyl-chain via the molclus [56] program. These conformers were initially optimized by density functional theory (DFT) calculations at the PM6-D3H4 [57] level through the MOPAC2016 [58] program, and then filtered and clustered using isostat tools of the molclus program. The resulting conformers were further optimized at the B97-D3/def2-SVP level with the resolution-of-identity approximation [59] using the ORCA 4.2 program [60]. Finally, conformers within 10 kcal/mol above the most stable conformer were extracted, aligned, and superimposed using the visual molecular dynamics (VMD) program [61]. Figure 2 shows that the distribution of alkyl-chains in the Y6 inadequately covers the donor core, and may cause transfer of the hole from the polymer donor to the donor core of the acceptor, thereby increasing the charge recombination. Contrarily, in the Y6-C2, the alkyl-chains cover the donor core more than in the Y6, aiding to prevent charge recombination on the acceptors. Regarding the Y6-C3, the alkyl-chains cover the donor core and some terminal acceptor parts, and this may hinder electron transfer from the polymer donor to the acceptor and the corresponding charge separation process. These results demonstrate that the Y6-C2 exhibits a more desirable alkyl-chains spatial distribution, that contributes to better device

Table 1 Optical and electrochemical properties of the Y6, Y6-C2, and Y6-C3

Acceptor	λ_{max}^{sol} (nm)	λ_{max}^{film} (nm)	λ_{onset}^{film} (nm)	E_g^{opt} a) (eV)	HOMO^{CV} (eV)	LUMO^{CV} (eV)	E_g^{cv} (eV)	μ_e (cm^2 V^{-1} s^{-1})
Y6	732	826	930	1.33	−5.67	−4.08	1.59	3.12×10^{-4}
Y6-C2	732	831	932	1.33	−5.65	−4.09	1.56	3.94×10^{-4}
Y6-C3	733	778	880	1.41	−5.68	−4.07	1.61	2.49×10^{-4}

a) Calculated from $E_g^{opt}=1240/\lambda_{onset}$.

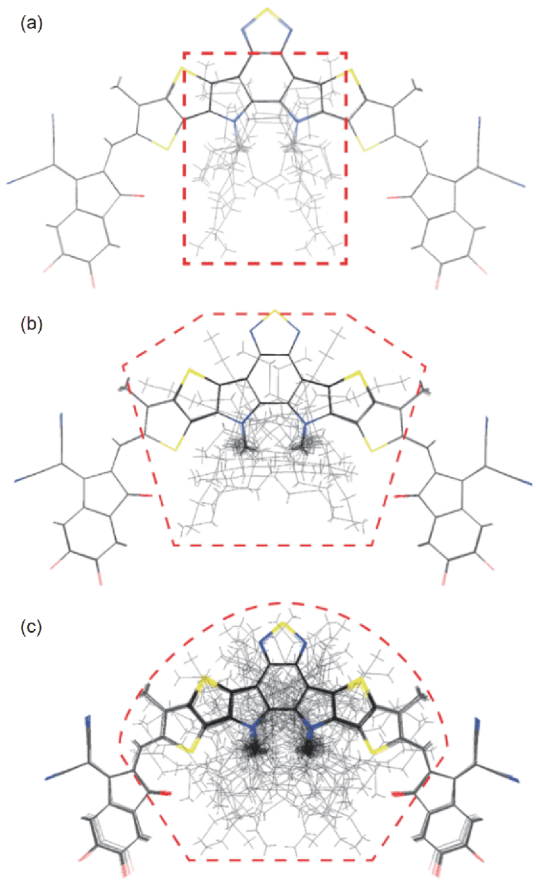

Figure 2 The superimposed stable conformers of (a) Y6, (b) Y6-C2, and (c) Y6-C3 calculated by DFT (color online).

performance.

The molecular ordering and crystalline properties of the neat acceptors were studied by GIWAXS experiments. Figure 3 reveals that the Y6 and Y6-C2 display favorable face-on stacking patterns relative to the substrate, while the Y6-C3 (longer alkyl-chains) exhibits the edge-on orientation, that is unfavorable for vertical charge transport and collection. Compared with the Y6, the Y6-C2 shows a stronger π-π stacking with q of 1.80 $Å^{-1}$ in the out-of-plane (OOP) direction and an enhanced crystal coherence length (CCL) (Y6=3.49 nm; Y6-C2=3.82 nm), suggesting a stronger π-π stacking propensity for the Y6-C2. In the in-plane (IP) direction, the Y6-C2 displays a well-developed (100) lamellar stacking peak (q=0.288 $Å^{-1}$) with a CCL of 8.13 nm and a d-spacing of 2.18 nm, also implying a stronger crystallization tendency. Therefore, the electron mobilities (μ_e) measured by the space-charge-limited current (SCLC) method for the Y6, Y6-C2, and Y6-C3 are 3.12×10^{-4}, 3.94×10^{-4}, and 2.49×10^{-4}, respectively (Figure S2). The highest electron mobility for the Y6-C2 is mainly attributed to its face-on dominant orientation and high CCL. These results indicate that altering the alkyl-chains branching points significantly influences the molecular orientation and crystallization propensity, and thus, the charge transport properties.

To assess the performance of the Y6, Y6-C2, and Y6-C3 as electron acceptors in OSCs, we paired them with the PM6 and fabricated bulk heterojunction (BHJ) OSCs with a conventional device structure of glass/ITO/PEDOT:PSS (poly(3,4-ethylenedioxythiophene):poly(styrene-sulfonate))/PM6:acceptors/PDINO (perylene diimide functionalized with amino N-oxide)/Al. The optimum as-cast active layers were achieved by spin-coating the PM:acceptor (1:1.2, w/w) blend solution with a total concentration of 16 mg mL^{-1} in the CF. The current density-voltage (J-V) characteristics are shown in Figure 4(a) and the corresponding photovoltaic parameters are presented in Table 2.

The as-cast OSCs based on the PM6:Y6 yields a PCE of 15.24%, with an open-circuit voltage (V_{OC}) of 0.859 V, a J_{SC} of 25.22 mA cm^{-2}, and an FF of 70.3%. Compared to the device based on the Y6, a higher PCE of 15.89% is recorded

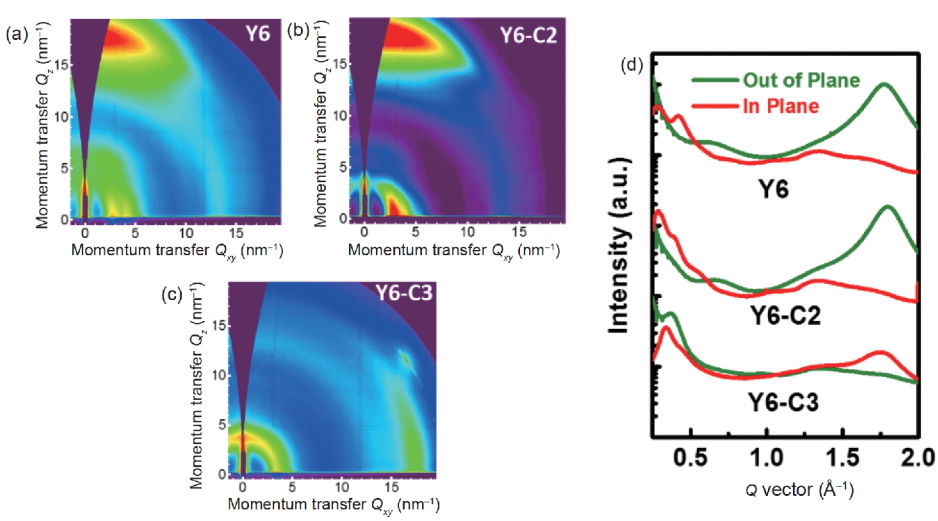

Figure 3 2D GIWAXS patterns of (a) Y6, (b) Y6-C2, and (c) Y6-C3 films. (d) The in-plane and out-of-plane line-cut profiles for the Y6, Y6-C2, and Y6-C3 films (color online).

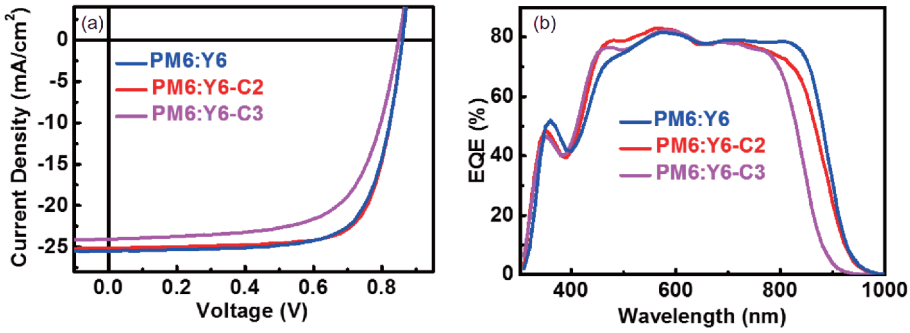

Figure 4 (a) *J-V* characteristics of the optimized as-cast OSCs at an illumination of AM 1.5G and 100 mW cm^{-2}. (b) The EQE spectra of the optimized as-cast devices based on the PM6:Y6, PM6:Y6-C2, and PM6:Y6-C3 (color online).

Table 2 Optimized photovoltaic performances for as-cast OSCs based on PM6/acceptors under standard AM 1.5G illumination and 100 mW cm^{-2}. The average values and standard deviations are based on 20 devices

Devices	V_{OC} (V)	J_{SC} (mA cm^{-2})	FF (%)	PCE (%)
PM6/Y6	0.859 (0.857±0.003)	25.22 (25.18±0.18)	70.3 (69.4±0.78)	15.24 (15.04±0.31)
PM6/Y6-C2	0.860 (0.858±0.003)	25.11 (25.06±0.22)	73.6 (73.0±0.67)	15.89 (15.64±0.27)
PM6/Y6-C3	0.852 (0.851±0.003)	24.07 (23.97±0.16)	67.4 (66.6±0.89)	13.76 (13.48±0.19)

for the device based on the PM6:Y6-C2, with a V_{OC} of 0.860, a J_{SC} of 25.11 mA cm^{-2}, and an FF of 73.6%. The higher PCE for the Y6-C2-based device is primarily ascribed to its higher FF. In contrast, based on the longest side chains, the Y6-C3-based device produced a PCE of 13.76%, representing the lowest value among the three acceptors, explained by its relatively low J_{SC} (24.07 mA cm^{-2}) and FF (67.1%). The PCE of 15.89% is the highest known value for as-cast nonfullerene OSCs reported (Table S1 in Supporting Information online). The integrated current densities from the external quantum efficiency (EQE) curves are 24.51 mA cm^{-2} for the PM6:Y6-C2-based devices, consistent with the *J-V* curves (within 3% error) (Figure 4(b)).

To further improve device performance, we utilized the PNDIT-F3N instead of the PDINO as the electron transport material, with 0.5% (vol) chloronaphthalene as the solvent additive, and a thermal annealing step at 100 °C for 5 min. Figure S3(a) and data Table S2 indicate that compared to the as-cast devices, the PCEs slightly increased for all devices mainly from enhanced FFs. Notably, the device based on the PM6:Y6-C2 affords a PCE of 16.28%, representing the best value among the three devices, and attributed to its highest FF. The J_{SC} integrated from the EQE spectra for the Y6-C2-based device is 24.86 mA cm^{-2} (Figure S3(b)), that is within a small error from the *J-V* measurements (J_{SC}= 25.64 mA cm^{-2}).

To understand the difference in FF for the three devices, we performed SCLC experiments on the three BHJ devices, as depicted in Figures S4, S5, and data in Table S3. Compared with devices based on the Y6 and Y6-C3, the Y6-C2-based device shows higher hole and electron mobilities (μ_h=12.2×10^{-4} cm^2 V^{-1} s^{-1} and μ_e=9.34×10^{-4} cm^2 V^{-1} s^{-1}), with a more balanced charge transport (μ_h/μ_e=1.31) that contributes to its higher FF. In addition, the photoinduced charge carrier extraction by a linearly increasing voltage (photo-CELIV) experiment was employed to further evaluate the carrier mobilities (Figure 5(a) and Figure S6) [62,63] and the average mobilities are presented in Table S4. The Y6-C2-based device displays a higher mobility (1.40×10^{-4} cm^2 V^{-1} s^{-1}) than the Y6-based (1.20×10^{-4} cm^2 V^{-1} s^{-1}) and Y6-C3-based (0.733×10^{-4} cm^2 V^{-1} s^{-1}) devices. Figure 5(b) illustrates that due to various recombination processes, the number of extracted carriers decreases as the delay time increases. Furthermore, using the following formula, $n(t) = \frac{n(0)}{1+\left(\frac{t}{\tau_B}\right)^{\gamma}}$, a bimolecular recombination coefficient (τ_B, also known as the effective 2nd order recombination coefficient) is calculated [64], where γ is the time-independent parameter and $n(0)$ is the density of the photogenerated carrier at t=0. Data for relevant parameters from fitting of the equation above are summarized in Table S2. The Y6-C2-based device shows a τ_B of 1.26×10^{-4} s, shorter than those of devices based on the Y6 (2.25×10^{-4} s) and Y6-C3 (3.39×10^{-4} s), indicating the weakest bimolecular recombination in the Y6-C2-based device. The transient time, t_{tr}, ($t_{tr} = \frac{L^2}{\mu V}$, where L is the thickness of active layer) values calculated are 1.66×10^{-7}, 1.43×10^{-7}, and 2.73×10^{-7} s for devices based on the Y6, Y6-C2, and Y6-C3, respectively. These results are consistent with the transient photocurrent

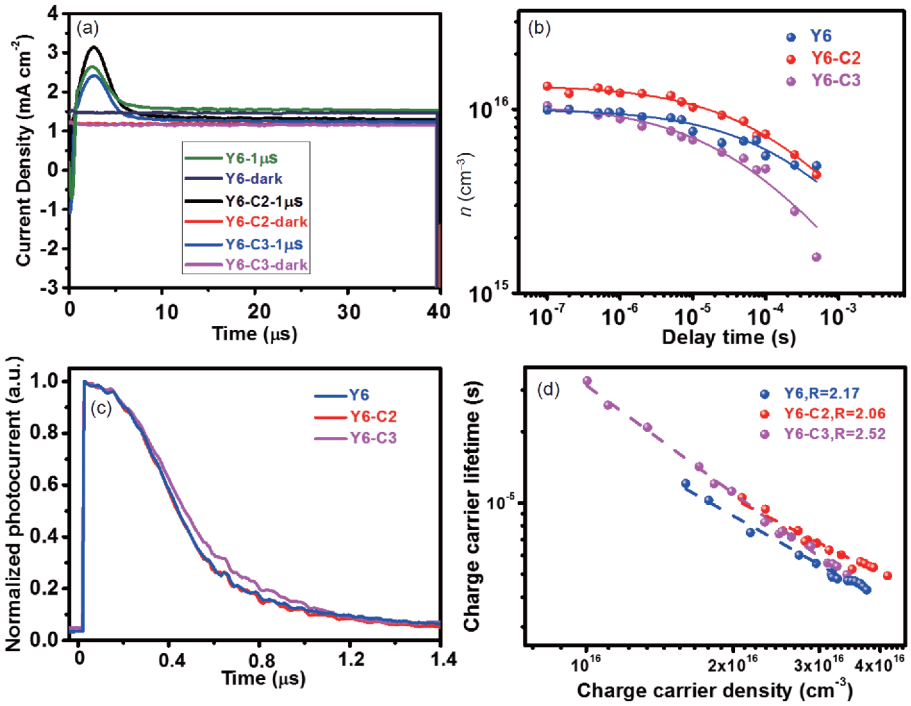

Figure 5 (a) The dark CELIV and photo-CELIV curves for the Y6-, Y6-C2-, and Y6-C3-based devices after a 1 μs delay. (b) Density of the extracted carrier as a function of the delay time and fit. (c) Normalized TPC curves for Y6-, Y6-C2-, and Y6-C3-based devices. The illumination pulse intensity is 150 mW cm^{-2} (a light pulse of 50 μs). (d) Charge carrier lifetime versus charge carrier density for Y6-, Y6-C2-, and Y6-C3-based devices (color online).

(TPC) (Figure 5(c)) and transient photovoltage (TPV) measurements (Figure S7). The TPC decay demonstrates that the photoinduced carrier sweep-out values in the PM6:Y6-C2 (0.31 μs) and PM6:Y6-based (0.32 μs) devices are faster than that for the PM6:Y6-C3-based (0.42 μs) device. Additionally, the charge carrier drift length (l_d) can be calculated by the following equation [65]: $l_d^{\,3} = \frac{\mu^2 U^2 e}{J_{SC}\beta}$, where β is the 2nd order recombination pre-factor and U is the assumed V_{OC} in the device. Data in Table S2 shows the longest carrier drift length (l_d=372 nm) for the PM6:Y6-C2-based device, implying that charges in the device cover longer distances (averagely) prior to recombination than the PM6:Y6 and PM6:Y6-C3 devices.

To further understand the carrier recombination in the three devices, we combined the charge extraction (Figure S8) and TPV techniques to obtain the charge carrier lifetime as a function of charge carrier density (Figure 5(d)). Generally, a recombination order R (R=λ+1, where λ is the recombination exponent) higher than 2 is ascribed to the effect of energetic and morphological traps [66]. The smallest R value of 2.05 is shown by the Y6-C2-based device (Figure 5(d)), highlighting the lowest amount of trap-assisted recombination. The low bimolecular recombination for the Y6-C2-based device is supported by the light intensity-dependent J_{SC} (Figure S9). The highest mobility, longest carrier drift length, and the smallest recombination order are consistent with the highest FF of the device.

To investigate the morphology of the blend films, we performed atomic force microscopy (AFM) and GIWAXS experiments. Figure 6 shows smooth and uniform surface morphologies from AFM height images for the blend films. The root-mean-square (RMS) roughness for the blend films are PM6:Y6 (0.603 nm), PM6:Y6-C2 (0.509 nm), and PM6:Y6-C3 (0.722 nm). The smallest RMS value shown by the PM6:Y6-C2-based blend reflects the most homogeneous morphology, capable of improving exciton dissociation. In addition, GIWAXS experiments were conducted to elucidate the molecular order and crystallization of the active layers. Regardless of the alkyl-chains branching points, the three blend films exhibited obvious (010) diffractions in the OOP direction and (100) diffractions in the IP direction, suggesting a preferential face-on stacking pattern, particularly for the PM6:Y6-C2-based blend. The peak area (010) and scattering intensity of the Y6- and Y6-C2-based blends are significantly higher than that for the Y6-C3-based blend, implying stronger crystallization/aggregation for the Y6 and Y6-C2 blend films. In the OOP direction, the PM6:Y6 and PM6:Y6-C2 blend films exhibit similar d-spacings (PM6:Y6=3.56 Å; PM6:Y6-C2=3.57 Å) and CCLs (PM6:Y6=3.169 nm; PM6:Y6-C2=3.170 nm). However, in the IP direction, the PM6:Y6-C2 blend film shows a narrower (100) peak than the PM6:Y6-based blend with a reduced full width at half-maximum (FWHM) (PM6:Y6=0.08745 Å; PM6:Y6-

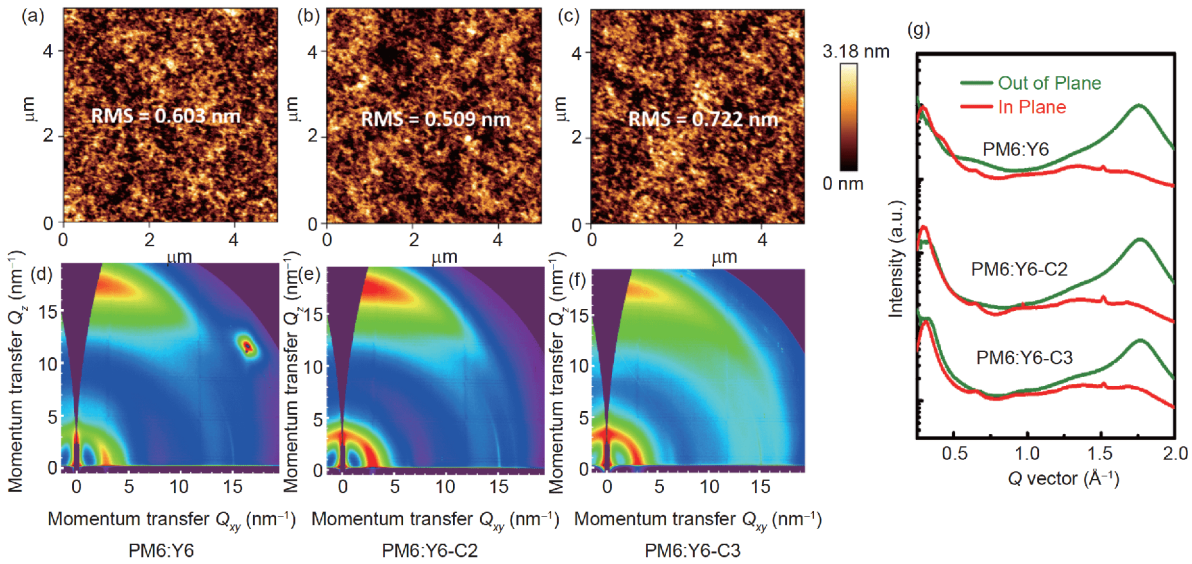

Figure 6 Representative AFM height images of (a) PM6:Y6, (b) PM6:Y6-C2, and (c) PM6:Y6-C3 blend films; 2D-GIWAXS patterns of (d) PM6:Y6, (e) PM6:Y6-C2, and (f) PM6:Y6-C3 blend films; (g) line-cut profiles of the GIWAXS patterns of PM6:Y6, PM6:Y6-C2, and PM6:Y6-C3 blend films (color online).

C2=0.08375 Å). The CCLs of the (100) peaks are 71.8 and 75.0 Å for PM6:Y6 and PM6:Y6-C2 films, respectively. The highly ordered structure and enhanced crystallization characteristics are beneficial for charge transport, with the highest FF for the PM6:Y6-C2-based device.

Considering the high efficiency of the Y6-C2-based as-cast OSCs, a large area (1.0 cm^{-2}) device (Figure 7(a)) was produced, with a PCE of 14.83% achieved, at a V_{OC} of 0.852 V, a J_{SC} of 24.36 mA cm^{-2}, and an FF of 71.5%, suggesting a major potential for large-scale industrial production for the PM6:Y6-C2 blend.

Furthermore, we evaluated the potential of the Y6-C2 in ternary OSCs. Recent research suggests incorporating a small fraction of $PC_{71}BM$ as the third component can further boost device performance for several high-performance binary systems, with potential to improve charge transport and reduce nonradiative energy loss. Thus, we fabricated ternary devices based on PM6:Y6-C2:$PC_{71}BM$ (1:1.0:0.2, weight ratio), producing a PCE up to 17.06%, with a V_{OC} of 0.859, a J_{SC} of 25.73 mA cm^{-2}, and an impressive FF of 77.2% (Figure 7(b)). The data in Table S5 indicates that the PCE and FF are the best results reported for ternary OSCs. Compared with the binary system, the improvement of the PCE in the ternary system is principally ascribed to the increased FF. To understand the FF enhancement from the binary to ternary system, a photo-CELIV experiment was employed to evaluate the carrier mobilities. Figure S10 reveals a higher mobility of 1.69×10^{-4} cm^2 V^{-1} s^{-1} for the PM6:Y6-C2:$PC_{71}BM$-based device relative to the PM6:Y6-C2-based device (1.40×10^{-4} cm^2 V^{-1} s^{-1}). Also, the Y6-C2-based ternary device exhibits a higher hole and electron mobility, with a more balanced μ_h/μ_e value relative to that for the Y6-C2-based binary device (Figure S11). In addition, the PM6:Y6-C2:$PC_{71}BM$-based device shows a slight larger $n(0)$ (1.10×10^{16} cm^{-3}) and smaller transient time (1.18×10^{-7} s), that are beneficial to the charge transport. Furthermore, we performed TPC measurements to investigate the carrier transport properties (Figure S12), with the TPC decay

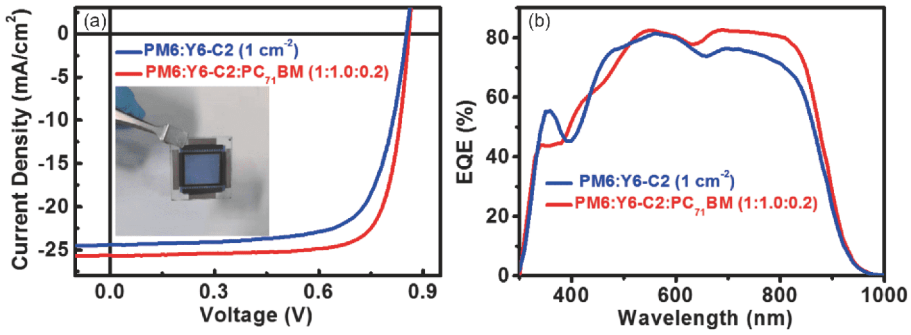

Figure 7 (a) The *J*-*V* curves and (b) the EQE spectra of the Y6-C2-based device with an area of 1.0 cm^2 and the PM6:Y6-C2:$PC_{71}BM$ (1:1.0:0.2) based ternary device (color online).

indicating that the photoinduced carrier sweep-out in the PM6:Y6-C2:$PC_{71}BM$-based ternary device (0.28 μs) are faster than the PM6:Y6-C3-based binary device (0.31 μs). The slightly smaller recombination order R (2.05) for the ternary device indicates a lower amount of trap-assisted recombination compared with the binary device (Figure S13). To better understand the mechanism for the enhancement from binary to ternary devices, we further studied the dark J-V curves (Figure S14). For the PM6:Y6-C2-based binary device and PM6:Y6-C2:$PC_{71}BM$-based ternary device, the J_{ph}s reaches saturation (J_{sat}) at high V_{eff} (i.e., V_{eff}≥2 V). At maximal power output and short-circuit conditions, the ratios of J_{ph}/J_{sat} are 85.8% and 97.3% for the Y6-C2-based binary device and 89.0% and 97.9% for the Y6-C2-based ternary device. The higher J_{ph}/J_{sat} implies that better charge collection and exciton dissociation occur in the Y6-C2-based ternary device. The enhanced charge carrier mobility and transport properties for the ternary device (1:1:0.2) reduces the charge recombination rate, that contributes to the increased FF value in such ternary devices. The J_{SC} integrated from the EQE spectrum of 25.12 mA cm^{-2} for the ternary device is consistent with the result from the J-V measurement.

3 Conclusions

Two new SMAs (Y6-C2 and Y6-C3) were designed and synthesized via by altering the alkyl-chains branching positions from the Y6 backbone. Compared with the Y6, the Y6-C2 exhibited similar absorption and electrochemical properties, but better molecular packing and enhanced crystallinity. However, for the Y6-C3, the longest side chains neat film was characterized by an obvious blue-shifted absorption compared to the Y6 and Y6-C2. Consequently, the as-cast Y6-C2-based device yielded a higher PCE of 15.89% those device based on the Y6 (15.24%) and Y6-C3 (13.76%). The superior PCE is attributed to its high FF associated with its highly ordered structure, better crystallization characteristics, longer carrier drift length, and lower recombination order of the PM6:Y6-C2 blend. Additionally, we obtained 14.83% efficiency for a PM6:Y6-C2-based device with an area of 1.00 cm^2. Importantly, the Y6-C2 showed good compatibility with the $PC_{71}BM$, enabling the demonstration of a ternary OSC device (PM6:Y6-C2:$PC_{71}BM$) with a high PCE (17.06%) and an impressive FF (0.772), representing the highest known values for ternary OSCs. These results demonstrate that modulation of the alkyl-chain branching point is an effective strategy for tuning the molecular packing and crystallization characteristics, This tuning highlights potential characteristics that can be exploited by the OSC community for developing high-performance SMAs.

Acknowledgements This work was supported by the National Natural Science Foundation of China (21572171, 21702154, 51773157, 51873160), the National Basic Research Program of China (2013CB834805), Shenzhen Peacock Plan (KQTD2017033011-0107046), Beijing National Laboratory for Molecular Sciences (BNLMS201905). We thank the Australian Synchrotron, part of ANSTO for partial work on the SAXS/WAXS beamline and the Supercomputing Center of Wuhan University for numerical work conducted using the supercomputing system.

Conflict of interest The authors declare that they have no conflict of interest.

Supporting information The supporting information is available online at http://chem.scichina.com and http://link.springer.com/journal/11426. The supporting materials are published as submitted, without typesetting or editing. The responsibility for scientific accuracy and content remains entirely with the authors.

1 Li G, Zhu R, Yang Y. *Nat Photon*, 2012, 6: 153–161
2 Lin Y, Zhan X. *Acc Chem Res*, 2016, 49: 175–183
3 Hou J, Inganäs O, Friend RH, Gao F. *Nat Mater*, 2018, 17: 119–128
4 Cheng P, Li G, Zhan X, Yang Y. *Nat Photon*, 2018, 12: 131–142
5 Yan C, Barlow S, Wang Z, Yan H, Jen AKY, Marder SR, Zhan X. *Nat Rev Mater*, 2018, 3: 18003
6 Lin Y, Zhan X. *Adv Energy Mater*, 2015, 5: 1501063
7 Baran D, Kirchartz T, Wheeler S, Dimitrov S, Abdelsamie M, Gorman J, Ashraf RS, Holliday S, Wadsworth A, Gasparini N, Kaienburg P, Yan H, Amassian A, Brabec CJ, Durrant JR, McCulloch I. *Energy Environ Sci*, 2016, 9: 3783–3793
8 Fan Q, Su W, Wang Y, Guo B, Jiang Y, Guo X, Liu F, Russell TP, Zhang M, Li Y. *Sci China Chem*, 2018, 61: 531–537
9 Kan B, Feng H, Yao H, Chang M, Wan X, Li C, Hou J, Chen Y. *Sci China Chem*, 2018, 61: 1307–1313
10 Chen H. *Sci China Chem*, 2019, 62: 403–404
11 Lin Y, Wang J, Zhang ZG, Bai H, Li Y, Zhu D, Zhan X. *Adv Mater*, 2015, 27: 1170–1174
12 Li Y. *Acc Chem Res*, 2012, 45: 723–733
13 Luo Z, Liu T, Chen Z, Xiao Y, Zhang G, Huo L, Zhong C, Lu X, Yan H, Sun Y, Yang C. *Adv Sci*, 2019, 6: 1802065
14 Che X, Li Y, Qu Y, Forrest SR. *Nat Energy*, 2018, 3: 422–427
15 Liu T, Luo Z, Fan Q, Zhang G, Zhang L, Gao W, Guo X, Ma W, Zhang M, Yang C, Li Y, Yan H. *Energy Environ Sci*, 2018, 11: 3275–3282
16 Gasparini N, Jiao X, Heumueller T, Baran D, Matt GJ, Fladischer S, Spiecker E, Ade H, Brabec CJ, Ameri T. *Nat Energy*, 2016, 1: 118
17 Zhou Z, Xu S, Song J, Jin Y, Yue Q, Qian Y, Liu F, Zhang F, Zhu X. *Nat Energy*, 2018, 3: 952–959
18 An Q, Zhang F, Zhang J, Tang W, Deng Z, Hu B. *Energy Environ Sci*, 2016, 9: 281–322
19 Sun R, Guo J, Sun C, Wang T, Luo Z, Zhang Z, Jiao X, Tang W, Yang C, Li Y, Min J. *Energy Environ Sci*, 2019, 12: 384–395
20 Liu T, Luo Z, Chen Y, Yang T, Xiao Y, Zhang G, Ma R, Lu X, Zhan C, Zhang M, Yang C, Li Y, Yao J, Yan H. *Energy Environ Sci*, 2019, 12: 2529–2536
21 Luo Z, Liu T, Wang Y, Zhang G, Sun R, Chen Z, Zhong C, Wu J, Chen Y, Zhang M, Zou Y, Ma W, Yan H, Min J, Li Y, Yang C. *Adv Energy Mater*, 2019, 9: 1900041
22 Jiang K, Wei Q, Lai JYL, Peng Z, Kim HK, Yuan J, Ye L, Ade H, Zou Y, Yan H. *Joule*, 2019, 3: 3020–3033
23 Yuan J, Zhang Y, Zhou L, Zhang G, Yip HL, Lau TK, Lu X, Zhu C, Peng H, Johnson PA, Leclerc M, Cao Y, Ulanski J, Li Y, Zou Y. *Joule*, 2019, 3: 1140–1151
24 Yang Y, Zhang ZG, Bin H, Chen S, Gao L, Xue L, Yang C, Li Y. *J Am Chem Soc*, 2016, 138: 15011–15018
25 Sun J, Ma X, Zhang Z, Yu J, Zhou J, Yin X, Yang L, Geng R, Zhu R,

Zhang F, Tang W. *Adv Mater*, 2018, 30: 1707150
26 Li Y, Zheng N, Yu L, Wen S, Gao C, Sun M, Yang R. *Adv Mater*, 2019, 31: 1807832
27 Sun H, Liu T, Yu J, Lau TK, Zhang G, Zhang Y, Su M, Tang Y, Ma R, Liu B, Liang J, Feng K, Lu X, Guo X, Gao F, Yan H. *Energy Environ Sci*, 2019, 12: 3328–3337
28 Cui Y, Yao H, Hong L, Zhang T, Xu Y, Xian K, Gao B, Qin J, Zhang J, Wei Z, Hou J. *Adv Mater*, 2019, 31: 1808356
29 Fan B, Zhang D, Li M, Zhong W, Zeng Z, Ying L, Huang F, Cao Y. *Sci China Chem*, 2019, 62: 746–752
30 Meng L, Zhang Y, Wan X, Li C, Zhang X, Wang Y, Ke X, Xiao Z, Ding L, Xia R, Yip HL, Cao Y, Chen Y. *Science*, 2018, 361: 1094–1098
31 Chang Y, Lau TK, Pan MA, Lu X, Yan H, Zhan C. *Mater Horiz*, 2019, 6: 2094–2102
32 Cui Y, Yao H, Zhang J, Zhang T, Wang Y, Hong L, Xian K, Xu B, Zhang S, Peng J, Wei Z, Gao F, Hou J. *Nat Commun*, 2019, 10: 2515
33 Hong L, Yao H, Wu Z, Cui Y, Zhang T, Xu Y, Yu R, Liao Q, Gao B, Xian K, Woo HY, Ge Z, Hou J. *Adv Mater*, 2019, 31: 1903441
34 Li K, Wu Y, Tang Y, Pan M-, Ma W, Fu H, Zhan C, Yao J. *Adv Energy Mater*, 2019, 9: 1901728
35 Yan T, Song W, Huang J, Peng R, Huang L, Ge Z. *Adv Mater*, 2019, 31: 1902210
36 Xu X, Feng K, Bi Z, Ma W, Zhang G, Peng Q. *Adv Mater*, 2019, 31: 1901872
37 Lin Y, Adilbekova B, Firdaus Y, Yengel E, Faber H, Sajjad M, Zheng X, Yarali E, Seitkhan A, Bakr OM, El-Labban A, Schwingenschlögl U, Tung V, McCulloch I, Laquai F, Anthopoulos TD. *Adv Mater*, 2019, 31: 1902965
38 Luo Z, Bin H, Liu T, Zhang ZG, Yang Y, Zhong C, Qiu B, Li G, Gao W, Xie D, Wu K, Sun Y, Liu F, Li Y, Yang C. *Adv Mater*, 2018, 30: 1706124
39 Gao W, Zhang M, Liu T, Ming R, An Q, Wu K, Xie D, Luo Z, Zhong C, Liu F, Zhang F, Yan H, Yang C. *Adv Mater*, 2018, 30: 1800052
40 Liu T, Gao W, Wang Y, Yang T, Ma R, Zhang G, Zhong C, Ma W, Yan H, Yang C. *Adv Funct Mater*, 2019, 29: 1902155
41 Liu T, Huo L, Chandrabose S, Chen K, Han G, Qi F, Meng X, Xie D, Ma W, Yi Y, Hodgkiss JM, Liu F, Wang J, Yang C, Sun Y. *Adv Mater*, 2018, 30: 1707353
42 Sun H, Tang Y, Koh CW, Ling S, Wang R, Yang K, Yu J, Shi Y, Wang Y, Woo HY, Guo X. *Adv Mater*, 2019, 31: 1807220
43 Xiao L, He B, Hu Q, Maserati L, Zhao Y, Yang B, Kolaczkowski MA, Anderson CL, Borys NJ, Klivansky LM, Chen TL, Schwartzberg AM, Russell TP, Cao Y, Peng X, Liu Y. *Joule*, 2018, 2: 2154–2166
44 Xu X, Yu T, Bi Z, Ma W, Li Y, Peng Q. *Adv Mater*, 2018, 30: 1703973
45 Luo Z, Sun C, Chen S, Zhang ZG, Wu K, Qiu B, Yang C, Li Y, Yang C. *Adv Energy Mater*, 2018, 8: 1800856
46 Bin H, Gao L, Zhang ZG, Yang Y, Zhang Y, Zhang C, Chen S, Xue L, Yang C, Xiao M, Li Y. *Nat Commun*, 2016, 7: 13651
47 Lin Y, He Q, Zhao F, Huo L, Mai J, Lu X, Su CJ, Li T, Wang J, Zhu J, Sun Y, Wang C, Zhan X. *J Am Chem Soc*, 2016, 138: 2973–2976
48 Feng S, Zhang C, Liu Y, Bi Z, Zhang Z, Xu X, Ma W, Bo Z. *Adv Mater*, 2017, 29: 1703527
49 Wang J, Wang W, Wang X, Wu Y, Zhang Q, Yan C, Ma W, You W, Zhan X. *Adv Mater*, 2017, 29: 1702125
50 Dou JH, Zheng YQ, Lei T, Zhang SD, Wang Z, Zhang WB, Wang JY, Pei J. *Adv Funct Mater*, 2014, 24: 6270–6278
51 Lei T, Dou JH, Pei J. *Adv Mater*, 2012, 24: 6457–6461
52 Meager I, Ashraf RS, Mollinger S, Schroeder BC, Bronstein H, Beatrup D, Vezie MS, Kirchartz T, Salleo A, Nelson J, McCulloch I. *J Am Chem Soc*, 2013, 135: 11537–11540
53 Zhang F, Hu Y, Schuettfort T, Di C, Gao X, McNeill CR, Thomsen L, Mannsfeld SCB, Yuan W, Sirringhaus H, Zhu D. *J Am Chem Soc*, 2013, 135: 2338–2349
54 Wang N, Zhan L, Li S, Shi M, Lau TK, Lu X, Shikler R, Li CZ, Chen H. *Mater Chem Front*, 2018, 2: 2006–2012
55 Li W, Chen M, Cai J, Spooner ELK, Zhang H, Gurney RS, Liu D, Xiao Z, Lidzey DG, Ding L, Wang T. *Joule*, 2019, 3: 819–833
56 Lu T. molclus program, Version 1.8.8, http://www.keinsci.com/research/molclus.html
57 Řezáč J, Hobza P. *J Chem Theor Comput*, 2012, 8: 141–151
58 MOPAC2016. HTTP://OpenMOPAC.net/, Version 2016, J.J.P. Stewart, Stewart Computational Chemistry, Colorado Springs, CO, USA
59 Neese F. *J Comput Chem*, 2003, 24: 1740–1747
60 Neese F. *WIREs Comput Mol Sci*, 2012, 2: 73–78
61 Humphrey W, Dalke A, Schulten K. *J Mol Graphics*, 1996, 14: 33–38
62 Baumann A, Lorrmann J, Rauh D, Deibel C, Dyakonov V. *Adv Mater*, 2012, 24: 4381–4386
63 Min J, Luponosov YN, Gasparini N, Richter M, Bakirov AV, Shcherbina MA, Chvalun SN, Grodd L, Grigorian S, Ameri T, Ponomarenko SA, Brabec CJ. *Adv Energy Mater*, 2015, 5: 1500386
64 Azimi H, Heumüller T, Gerl A, Matt G, Kubis P, Distaso M, Ahmad R, Akdas T, Richter M, Peukert W, Brabec CJ. *Adv Energy Mater*, 2013, 3: 1589–1596
65 Clarke TM, Rodovsky DB, Herzing AA, Peet J, Dennler G, DeLongchamp D, Lungenschmied C, Mozer AJ. *Adv Energy Mater*, 2011, 1: 1062–1067
66 Min J, Güldal NS, Guo J, Fang C, Jiao X, Hu H, Heumüller T, Ade H, Brabec CJ. *J Mater Chem A*, 2017, 5: 18101–18110